

Topological Phase Transitions in Disordered Electric Quadrupole Insulators

Chang-An Li,^{1,2} Bo Fu,³ Zi-Ang Hu,³ Jian Li,^{1,2,*} and Shun-Qing Shen^{4,†}

¹*School of Science, Westlake University, 18 Shilongshan Road, Hangzhou 310024, Zhejiang Province, China*

²*Institute of Natural Sciences, Westlake Institute for Advanced Study,
18 Shilongshan Road, Hangzhou 310024, Zhejiang Province, China*

³*Department of Physics, The University of Hong Kong, Pokfulam Road, Hong Kong, China*

⁴*Department of Physics, The University of Hong Kong, Pokfulam Road, Hong Kong, China*

(Dated: December 2, 2021)

We investigate disorder-driven topological phase transitions in quantized electric quadrupole insulators. We show that chiral symmetry can protect the quantization of the quadrupole moment q_{xy} , such that the higher-order topological invariant is well-defined even when disorder has broken all crystalline symmetries. Moreover, nonvanishing q_{xy} and consequent corner modes can be induced from a trivial insulating phase by disorder that preserves chiral symmetry. The critical points of such topological phase transitions are marked by the occurrence of extended boundary states even in the presence of strong disorder. We provide a systematic characterization of these disorder-driven topological phase transitions from both bulk and boundary descriptions.

Introduction.- Disorder is ubiquitous in condensed matter systems. A wide range of fundamental phenomena, such as the Anderson localization and the Kondo effect [1–6], are closely related to disordered systems. When disorder is included in the study of topological phases of matter [7, 8], the surprising phenomenon of topological Anderson insulators will occur [9–14], which showcases a nontrivial interplay between disorder and topology. Recently, the concept of topological invariants in solids has been generalized to higher orders [15–42]. These higher-order topological insulators, like their conventional cousins, possess boundary states dictated by bulk topological invariants, but only at even lower dimensions than the latter. Among the higher-order topological phases, the quantized electric quadrupole insulator (QEIQ) is a prototypical one that features a quantized electric quadrupole moment in the bulk and zero-energy modes at the corners [15, 16]. From the outset, a QEIQ has been considered as a topological crystalline insulator [43, 44], where the quantization of its electric quadrupole moment is protected by the underlying crystalline symmetries [16]. This apparently poses a no-go condition for the existence of any nontrivial effect induced by disorder in such a system, where all the crystalline symmetries are bound to be broken. As such, a systematic study of the disorder effect in QEIQs, especially its resultant topological phase transitions, remains an open problem despite some related efforts [45–49].

In this work, we first prove that the electric quadrupole moment will remain quantized in the presence of disorder, as long as a chiral symmetry is preserved in the system. This allows us to investigate well-defined topological phases in disordered QEIQs. We found that disorder generically introduces a deformation of the phase diagram from the clean limit of a QEIQ (see Fig. 1a). This deformation is nontrivial in the sense that the topological phase regime can expand due to disorder in certain parameter space (see Fig. 1b). The disordered phase

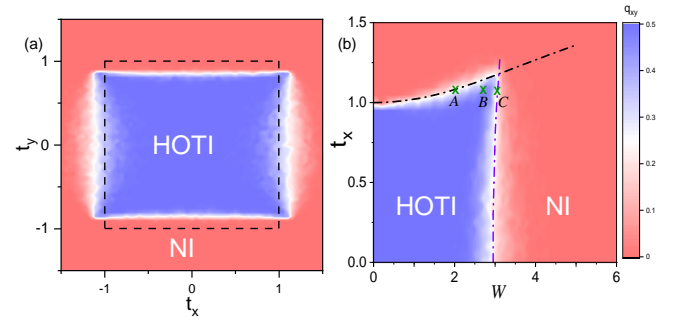


Figure 1. Phase diagrams of disordered electric quadrupole insulators. (a) Electric quadrupole moment q_{xy} as a function of mass parameters t_x and t_y at a fixed disorder strength $W = 2.5$. The dashed lines indicate the phase boundaries in the clean limit. (b) q_{xy} as a function of t_x and W at fixed $t_y = 0.8$. The dot-dashed lines are the phase boundaries obtained from an effective medium theory. In these phase diagrams, the disorder is of the $V(\mathbf{r})\gamma_4$ type, with 120/150 random configurations averaged in (a)/(b). The system is of size $L_x \times L_y = 30 \times 30$ with periodical boundary conditions.

diagrams can be analyzed accurately by using the effective medium theory for the bulk, despite the fact that the topological phase transitions bear no signature in the bulk energy spectrum. Indeed, as an unusual feature of higher-order topological phases, a disorder-induced transition between distinct phases is marked by a localization-delocalization-localization (LDL) transition on specific parts of the system boundary, which leads to a redistribution of fractional charges at the corners of a QEIQ. We demonstrate this picture explicitly by combining finite-size scaling analyses with exactly obtained charge densities.

Quantized electric quadrupole moments q_{xy} protected by chiral symmetry.- We consider the following effective

Bloch Hamiltonian for a QEQI [15, 16]:

$$H_q(\mathbf{k}) = t \sin k_y \gamma_1 + [t_y + t \cos k_y] \gamma_2 + t \sin k_x \gamma_3 + [t_x + t \cos k_x] \gamma_4, \quad (1)$$

where the gamma matrices are defined as $\gamma_j = -\tau_2 \sigma_j$ ($j = 1, 2, 3$) and $\gamma_4 = \tau_1 \sigma_0$ with τ and σ both being Pauli matrices but for different degrees of freedom; $k_{x/y}$ is the wave-vector along x/y (we have set the lattice constant to be unit). The bulk bands of Eq. (1) are gapped unless $|t_x| = |t_y| = |t|$. Without loss of generality, we will set $t = 1$ hereafter. This model respects chiral symmetry $\gamma_5^{-1} H_q(\mathbf{k}) \gamma_5 = -H_q(\mathbf{k})$, where the chiral symmetry operator $\gamma_5 \equiv -\gamma_1 \gamma_2 \gamma_3 \gamma_4 = \tau_3 \sigma_0$. Since k_x and k_y are decoupled in Eq. (1), the total Hamiltonian can be recast as the sum of two Su-Schrieffer-Heeger (SSH) models along two directions as $H_q(\mathbf{k}) = H_x(k_x) + H_y(k_y)$. In the clean limit, the topologically nontrivial phase is constrained in the region $|t_{s=x,y}| < 1$ where both $H_x(k_x)$ and $H_y(k_y)$ are topologically nontrivial. Under this condition, if an open boundary with a right-angle corner is considered, we can solve the corner state wavefunction to be of the form $\Psi_c(x, y) = \chi_c \phi_x(x) \phi_y(y)$, where ϕ_x and ϕ_y are two scalar functions, and χ_c is an eigenstate of the chiral symmetry operator: $\gamma_5 \chi_c = \pm \chi_c$ [50].

When disorder is introduced into the system, the first question we encounter is whether, or when, the electric quadrupole moment will remain quantized, such that a disordered QEQI phase can be well-defined. This question is particularly relevant because QEQIs have been constructed as topological crystalline insulators from the outset, where mirror symmetries are required to ensure the quantization of the electric quadrupole moment. In addition, the nested Wilson loop approach [16] originally used to obtain the topological invariant from the momentum space is no longer applicable in the disordered systems. Here, we prove that the quadrupole moment defined in the real space, given by [51–53]

$$q_{xy} = \frac{1}{2\pi} \text{Im} \log \left[\det(U^\dagger \hat{Q} U) \sqrt{\det(\hat{Q}^\dagger)} \right], \quad (2)$$

is indeed quantized even in the presence of disorder as long as the chiral symmetry is preserved. In the above equation: $\hat{Q} \equiv \exp[i2\pi \hat{q}_{xy}]$ and $\hat{q}_{xy} \equiv \hat{x} \hat{y} / (L_x L_y)$ with $\hat{x}(\hat{y})$ the position operator along the $x(y)$ dimension and $L_{x,y}$ the corresponding size; $\sqrt{\det(\hat{Q}^\dagger)} = \exp[-i\pi \text{Tr} \hat{q}_{xy}]$; the matrix U is constructed by column-wise packing all the occupied eigenstates, such that UU^\dagger is the projector to the occupied subspace.

We sketch our proof as follows and leave the full detail in Supplemental Materials [50]. For q_{xy} to be quantized as an integer multiple of $1/2$, clearly $\det(U^\dagger \hat{Q} U) \sqrt{\det \hat{Q}^\dagger}$ has to be real. By using Sylvester's determinant identity $\det(\mathbf{1} + AB) = \det(\mathbf{1} + BA)$, and the identity

$UU^\dagger + VV^\dagger = \mathbf{1}$ with VV^\dagger the projector to the unoccupied subspace (V is constructed from the unoccupied eigenstates similar to U), we obtain $\det(U^\dagger \hat{Q} U) = \det(V^\dagger \hat{Q}^\dagger V) \det \hat{Q}$. Noticing that the chiral symmetry operator relates the occupied states with unoccupied states by $V = \gamma_5 U$, as well as the fact that $[\gamma_5, \hat{Q}] = 0$, we have

$$\det(U^\dagger \hat{Q} U) = \det(U^\dagger \hat{Q}^\dagger U) \det \hat{Q}. \quad (3)$$

Since \hat{Q} is unitary, it follows immediately that $\det(U^\dagger \hat{Q} U) \sqrt{\det \hat{Q}^\dagger}$ is real. In other words, q_{xy} is quantized to be 0 or $1/2$ as long as the system preserves the chiral symmetry [50]. Note that, in this proof, the explicit form of \hat{Q} is irrelevant except for its commutativity with the chiral symmetry operator, which is generally true because the chiral symmetry is a local symmetry (i.e., diagonal in terms of real-space degrees of freedom) whereas \hat{Q} is constructed from position operators only. Therefore, the conclusion of this proof can be straightforwardly generalized by replacing \hat{Q} with other functions of position operators such as the electric octupole moment operator [15, 16]. In the Supplemental Materials [50], we further show how to generalize this proof to the case of particle-hole symmetry [53], which is also a local symmetry but does not commute with \hat{Q} because of its anti-unitary nature.

Phase diagram of disordered electric quadrupole insulators.— With a well-defined topological invariant established for disordered QEQIs, we now present the resulting phase diagrams based on the model in Eq. (1). To be specific, we choose one particular type of disorder that preserves the chiral symmetry, represented by $V_{\text{dis}} = V(\mathbf{r}) \gamma_4$ with the random function $V(\mathbf{r})$ distributed uniformly within the interval $[-W/2, W/2]$ and W being the disorder strength. The averaged quadrupole moment q_{xy} of disordered QEQIs as a function of t_x and t_y is shown in Fig. 1(a). Two separate phases can be clearly distinguished: one with $q_{xy} = 1/2$ (in blue) signifying a nontrivial higher-order topological insulator (HOTI) phase, and the other with $q_{xy} = 0$ (in red) signifying a trivial normal insulator (NI) phase. This phase diagram is more informative when compared with the phase diagram in the clean limit, the phase boundary of which has been marked by dashed lines also in Fig. 1(a). There are obviously contrasting behaviors in terms of the deformation of the HOTI phase regime in the two parameter dimensions (t_x and t_y) caused by disorder: the HOTI phase occurs in a shrunk range in t_y but an expanded range in t_x — the chosen type of disorder is coupled to the same gamma matrix γ_4 with the latter parameter but not the former one. A more precise analysis of how the deformed phase boundary relies on the disorder type and strength will be given in the next section by employing the effective medium theory and the self-consistent Born approximation (SCBA). Before that, we examine more closely the disorder induced expansion of the nontrivial HOTI phase in the parameter space t_x .

In Fig. 1(b) we show the phase diagram in the W - t_x space with fixed t_y . We notice again two types of phase boundaries, marked by a black (upper) and a purple (right-side) dot-dashed line, respectively. The upper phase boundary exhibits a clear monotonic increase of the critical t_x with stronger disorder W , corresponding to the expanded t_x range by disorder for the HOTI phase in Fig. 1(a), until it intersects with the right-side phase boundary. As we are set to show in the next section, the right-side phase boundary, which puts an upper bound of the disorder strength for the HOTI phase, originates from the constraint imposed by the disorder-renormalized t_y that has also led to the shrunk range of t_y for the HOTI phase in Fig. 1(a). These two phase boundaries represent exactly the topological phase transitions that are central to this paper.

Effective medium theory of the disorder-induced topological phase transitions.— A better understanding of the disorder-induced topological phase transitions can be achieved with the help of an effective medium theory and the SCBA method [54–57]. In the SCBA method, the key is to obtain the self-energy introduced by the disorder self-consistently, and then to include the self-energy as renormalization to the original Hamiltonian. In our case, by symmetry arguments the self-energy can be simplified to be

$$\Sigma(E_F) = \Sigma_4\gamma_4 + \Sigma_2\gamma_2 + \Sigma_0 I_{4\times 4}. \quad (4)$$

Specifically, the self-energy Σ satisfies the following self-consistent integral equation

$$\Sigma(E_F) = \frac{W^2}{48\pi^2} \int_{BZ} d^2\mathbf{k} \gamma_4 \frac{1}{E_F + i\eta - H_q(\mathbf{k}) - \Sigma(E_F)} \gamma_4, \quad (5)$$

where the integral runs over the first Brillouin zone, and η is an infinitesimal positive number. E_F is Fermi energy which is set at zero here, i.e., the system is half filled. From Eq. (S3.5), there are explicitly three coupled self-consistent integral equations that will fully determine Σ [50]. After obtaining the self-energy Σ (where Σ_0 turns out to be zero at zero energy because of the chiral symmetry), the topological mass terms t_x and t_y are renormalized according to

$$\bar{t}_x = t_x + \text{Re}\Sigma_4, \quad (6a)$$

$$\bar{t}_y = t_y + \text{Re}\Sigma_2. \quad (6b)$$

This produces the new phase boundaries at $|\bar{t}_x| = |\bar{t}_y| = 1$, which formally resemble the conditions in the clean limit but with a key difference in the implicit dependence on W .

The preceding approach can quantitatively account for the phase boundaries in the presence of disorder. The expanded range of t_x and the shrunk range of t_y for the HOTI phase in the disordered phase diagram, as shown in Fig. 1(a), can be understood from the opposite signs

of the self-energy contributions Σ_4 and Σ_2 , which in turn comes from the anti-commutation relation between γ_4 and γ_2 [50]. In previous discussions, we have seen that only if the two individual SSH models consisting the full model in Eq. (1) are topologically nontrivial simultaneously, the system can possess nontrivial bulk topological invariant and host zero-energy modes at its corners. Therefore, if disorder drives one of the two SSH components from topologically nontrivial to trivial, a phase transition of the higher-dimensional system will occur. Indeed, the topological phase transitions of the two SSH components are each captured by one of the conditions $|\bar{t}_{x,y}| = 1$ with the renormalized mass $\bar{t}_{x,y}(t_{x,y}, W)$ given by Eq. (6). For a fixed disorder strength W , such as in the case shown in Fig. 1(a), these conditions lead to four critical values of t_x and t_y , resulting in a rectangular shaped phase boundary in the phase diagram. With varying disorder strength, on the other hand, the two conditions lead directly to the two phase boundary lines demonstrated in Fig. 1(b). Specifically, we plot the solutions to the equations $\bar{t}_x = 1$ and $\bar{t}_y = 1$ as the dot-dashed lines in black and in purple, respectively. Both lines coincide very well with the phase boundaries obtained from numerically calculating q_{xy} as discussed in previous sections, until the two lines intersect.

Localization-delocalization-localization transitions at open boundaries.— The higher-order topological phase transitions generically show no signatures in terms of the bulk energy spectrum but instead are accompanied by LDL transitions at the open boundaries of the system. To demonstrate this in disordered systems, we perform a finite size scaling analysis based on localization length calculated from the numerical transfer matrix method [50, 58–60]. Specifically, we compare the localization length (at zero energy) along quasi-one-dimensional ribbons of our model system with different width, longitudinal orientations and transverse boundary conditions. The dependence of the localization length on the ribbon width, in a specific orientation and boundary condition setting, indicates the presence or absence of delocalized bulk or boundary states in the thermodynamic limit. We focus on the parameter space close to the phase boundaries identified in the previous sections. With a periodic boundary condition in the transverse dimension, we found that the localization length (upon normalization by the width) decrease monotonically with increasing width in the entire parameter ranges of our interest, regardless of the orientation along the ribbon [50]. This indicates that there is no occurrence of delocalized bulk states during the phase transitions — the bulk of the system remains insulating. In contrast, when an open boundary condition is considered, the localization length along certain longitudinal orientation can exhibit monotonic increase with increasing width, signifying a divergence in the thermodynamic limit, around a topological phase transition point, as exemplified in Fig. 2(a, b).

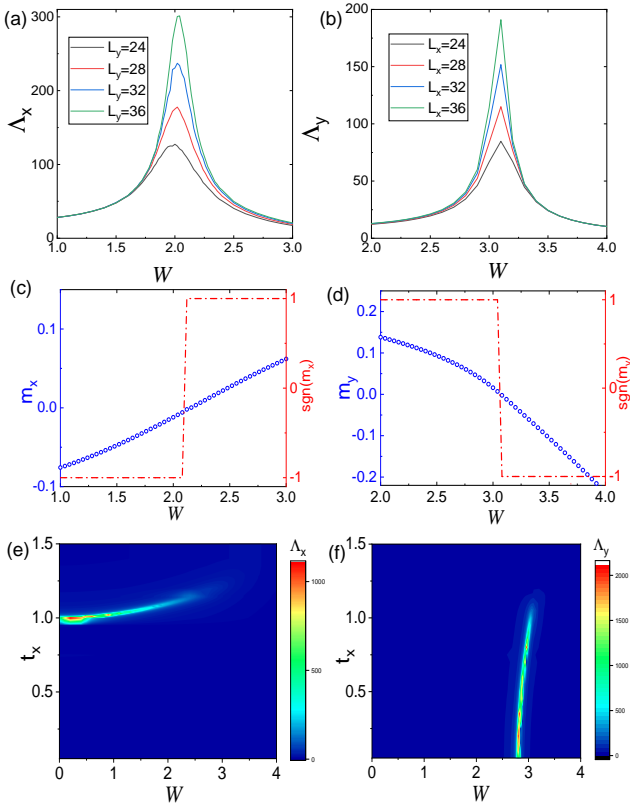


Figure 2. Signatures of delocalized states at the open boundaries: a finite-size scaling analysis of the localization length (a) Λ_x and (b) Λ_y as functions of W with an open boundary condition in the transverse dimension; effective boundary mass terms (c) m_x and (d) m_y as functions of W ; phase boundaries indicated by the divergence of (e) Λ_x and (f) Λ_y as analyzed in the (a) and (b) panels. In panels (a-d), we have set $t_x = 1.1$ and $t_y = 0.8$.

The divergence of the localization length at a critical value of the disorder strength, which occurs only with an open boundary condition and along certain orientation, indicates the existence of delocalized states at the corresponding boundaries, despite strong disorder, at the critical point. We note that the LDL transitions discussed here are similar to the topological phase transitions across Landau levels in the quantum Hall effect [61], in the fact that the delocalized states occur only at the exact critical points.

The boundary LDL transitions established above by a finite-size scaling analysis can be further understood with an effective boundary theory [50], where the (boundary) spectrum around a critical point is controlled by an effective mass, given by $m_x = 1 - t_x - \text{Re}[\Sigma_4(W)]$ for the boundaries along x , or $m_y = 1 - t_y - \text{Re}[\Sigma_2(W)]$ for the boundaries along y . The critical points are associated with the conditions $m_{x,y} = 0$, which coincide with the conditions that we have derived earlier from the bulk phase transitions. By using the SCBA method, the ef-

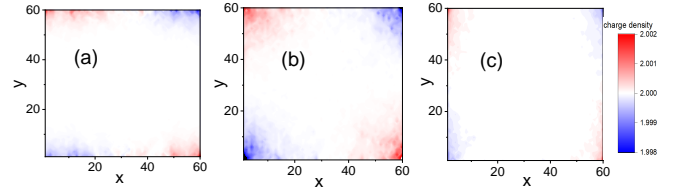


Figure 3. Charge density distributions (a, b, c) that correspond to the three points, A, B, and C, (marked by crosses) in the phase diagram in Fig. 1(b). The points A and C sit in different phase boundaries; the point B sits inside the non-trivial QEQI phase. The values of the disorder strength in (a), (b), and (c) are $W = 2.02$, $W = 2.70$ and $W = 3.10$, respectively. In all these calculations we have set $t_x = 1.1$ and $t_y = 0.8$, and taken an average of 10 disorder configurations.

fective mass values and corresponding signs are obtained and shown in Figs. 2(c, d), which agree with the finite-size scaling results.

The LDL transitions along each open boundary orientation also enable us to establish the two types of phase boundaries discussed previously in the context of bulk topology. This is shown in Figs. 2(e, f) with calculated localization length corresponding to Figs. 2(a, b). The full agreement between this approach and the bulk invariant approach manifests the close interconnection between the boundary and the bulk descriptions of the higher-order topological phase transitions.

Charge density redistribution at boundaries and corners.- A hallmark of QEQIs is the presence of fractional charges at the corners which consist in the quantized electric quadrupole. In this section we demonstrate how the disorder-driven topological phase transitions lead to the redistribution of the charge density towards (or away from) the fractional corner charges. For clarity and simplicity, let us focus on three representative points in the phase diagram, marked by A, B, and C in Fig. 1(b). These three phase points correspond to a fixed t_x (we choose $t_x = 1.1$) but varying disorder strength W , such that A and C sit on the two types of phase boundaries respectively, whereas B sits in the non-trivial QEQI phase. The calculated charge densities for these points are shown in Fig. 3. At the critical point A(C'), the charge density extends only along the $x(y)$ boundaries, as enabled by the occurrence of delocalized states thereat, and exhibits a continuous bipolar form with opposite polarities (offset by the mean values) on opposite boundaries; at the B point, the charge density displays a more symmetric quadrupolar form that is deformed from the dipoles in A or C. The charge density in the B point shows clear localization at the corners owing to the topological bulk-corner correspondence, and upon integration over each quadrant sums to the fractional value $\pm 1/2$ with high accuracy when the system size is sufficiently large.

Conclusion.- In short, we have presented a compre-

hensive description of the disorder-induced topological phase transitions in quantized electric quadrupole insulators. It is proved rigorously that the quantization of the electric quadrupole moment q_{xy} can be protected by the chiral symmetry even in the presence of strong disorder. We have also uncovered disorder-driven phase transitions from trivial to higher-order topological phases, which are signified by localization-delocalization-localization transitions at certain open boundaries with the system bulk remaining insulating. We expect this exotic disorder effect can be experimentally demonstrated in, e.g., photonic crystals [38–40] or electric circuits [36, 37] by taking advantage of their high controllability.

C. A. Li thanks Liyuan Chen and A. Weststrom for helpful discussions, and acknowledges B. Kang and G. Y. Cho for communication on the real part of quadrupole formula. This work was supported by NSFC under Grants No. 11774317, NSF of Zhejiang under Grant No. Q20A04005, and the Research Grants Council, University Grants Committee, Hong Kong under Grants Nos. 17301717 and 17301220. The numerical calculations were performed on Supercomputer cluster of Westlake University.

* lijian@westlake.edu.cn

† sshen@hku.hk

- [1] P. A. Lee and T. V. Ramakrishnan, *Disordered electronic systems*, Rev. Mod. Phys. **57**, 287 (1985)
- [2] P. W. Anderson, *Absence of Diffusion in Certain Random Lattices*, Phys. Rev. **109**, 1492 (1958).
- [3] F. Evers and A. D. Mirlin, *Anderson transitions*, Rev. Mod. Phys. **80**, 1355 (2008).
- [4] L. Sanchez-Palencia and M. Lewenstein, *Disordered quantum gases under control*, Nat. Phys. **6**, 87 (2010).
- [5] J. Kondo, *Resistance Minimum in Dilute Magnetic Alloys*, Prog. Theor. Phys. **32**, 37 (1964).
- [6] A. C. Hewson, *The Kondo Problem to Heavy Fermions*, (Cambridge University Press, Cambridge, 1997).
- [7] M. Z. Hasan and C. L. Kane, *Colloquium: Topological insulators*, Rev. Mod. Phys. **82**, 3045 (2010).
- [8] X.-L. Qi and S.-C. Zhang, *Topological insulators and superconductors*, Rev. Mod. Phys. **83**, 1057 (2011).
- [9] J. Li, R.-L. Chu, J. K. Jain, and S.-Q. Shen, *Topological Anderson insulator*, Phys. Rev. Lett. **102**, 136806 (2009).
- [10] H. Jiang, L. Wang, Q.-f. Sun, and X. C. Xie, *Numerical study of the topological Anderson insulator in HgTe/CdTe quantum wells*, Phys. Rev. B **80**, 165316 (2009).
- [11] H.-M. Guo, G. Rosenberg, G. Refael, and M. Franz, *Topological Anderson Insulator in Three Dimensions*, Phys. Rev. Lett. **105**, 216601 (2010).
- [12] I. Mondragon-Shem, T. L. Hughes, J. Song, and E. Prodan, *Topological criticality in the chiral-symmetric AIII class at strong disorder*, Phys. Rev. Lett. **113**, 046802 (2014).
- [13] E. J. Meier, F. A. An, A. Dauphin, M. Maffei, P. Massignan, T. L. Hughes, and B. Gadway, *Observation of the topological Anderson insulator in disordered atomic wires*, Science **362**, 929 (2018).
- [14] S. Stutzer, Y. Plotnik, Y. Lumer, P. Titum, N. H. Lindner, M. Segev, M. C. Rechtsman, and A. Szameit, *Photonic topological Anderson insulators*, Nature **560**, 461 (2018).
- [15] W. A. Benalcazar, B. A. Bernevig, and T. L. Hughes, *Quantized electric multipole insulators*, Science **357**, 61 (2017).
- [16] W. A. Benalcazar, B. A. Bernevig, and T. L. Hughes, *Electric multipole moments, topological multipole moment pumping, and chiral hinge states in crystalline insulators*, Phys. Rev. B **96**, 245115 (2017).
- [17] F. Schindler, A. M. Cook, M. G. Vergniory, Z. Wang, S. S. P. Parkin, B. A. Bernevig, and T. Neupert, *Higher-order topological insulators*, Sci. Adv. **4**, 6 (2018).
- [18] J. Langbehn, Y. Peng, L. Trifunovic, F. von Oppen, and P. W. Brouwer, *Reflection-symmetric second-order topological insulators and superconductors*, Phys. Rev. Lett. **119**, 246401 (2017).
- [19] Y. Peng, Y. Bao, and F. von Oppen, *Boundary Green functions of topological insulators and superconductors*, Phys. Rev. B **95**, 235143 (2017).
- [20] Z. Song, Z. Fang, and C. Fang, *(d-2)-dimensional edge states of rotation symmetry protected topological states*, Phys. Rev. Lett. **119**, 246402 (2017).
- [21] E. Khalaf, *Higher-order topological insulators and superconductors protected by inversion symmetry*, Phys. Rev. B **97**, 205136 (2018).
- [22] Y. You, T. Devakul, F. J. Burnell, and T. Neupert, *Higher-order symmetry-protected topological states for interacting bosons and fermions*, Phys. Rev. B **98**, 235102 (2018).
- [23] M. Geier, L. Trifunovic, M. Hoskam, and P. W. Brouwer, *Second-order topological insulators and superconductors with an order-two crystalline symmetry*, Phys. Rev. B **97**, 205135 (2018).
- [24] M. Ezawa, *Higher-order topological insulators and semimetals on the breathing kagome and pyrochlore lattices*, Phys. Rev. Lett. **120**, 026801 (2018).
- [25] S. Franca, J. van den Brink, and I. C. Fulga, *An anomalous higher-order topological insulator*, Phys. Rev. B **98**, 201114(R) (2018).
- [26] R. Okugawa, S. Hayashi, and T. Nakanishi, *Second-order topological phases protected by chiral symmetry*, Phys. Rev. B **100**, 235302 (2019).
- [27] Z. Wang, B. J. Wieder, J. Li, B. Yan, and B. A. Bernevig, *Higher-order topology, monopole nodal lines, and the origin of large Fermi arcs in transition metal dichalcogenides XTe₂*, Phys. Rev. Lett. **123**, 186401 (2019).
- [28] K. Kudo, T. Yoshida, and Y. Hatsugai, *Higher-order topological mott insulators*, Phys. Rev. Lett. **123**, 196402 (2019).
- [29] M. J. Park, Y. Kim, G. Y. Cho, and S. B. Lee, *Higher-order topological insulator in twisted bilayer graphene*, Phys. Rev. Lett. **123**, 216803 (2019).
- [30] H. Li, and K. Sun, *Pfaffian formalism for higher-order topological insulators*, Phys. Rev. Lett. **124**, 036401 (2020).
- [31] L. Trifunovic and P. W. Brouwer, *Higher-order bulk-boundary correspondence for topological crystalline phases*, Phys. Rev. X **9**, 011012 (2019).
- [32] L. Trifunovic and P. W. Brouwer, *Higher-order topological band structures*, arXiv:2003.01144.

- [33] I. Petrides and O. Zilberberg, *Higher-order topological insulators, topological pumps and the quantum Hall effect in high dimensions*, Phys. Rev. Research **2**, 022049(R)(2020).
- [34] F. Schindler, Z. Wang, M. G. Vergniory, A. M. Cook, A. Murani, S. Sengupta, A. Y. Kasumov, R. Deblock, S. Jeon, I. Drozdov, H. Bouchiat, S. Gueon, A. Yazdani, B. A. Bernevig, and T. Neupert, *Higher-order topology in bismuth*, Nat. Phys. **14**, 918 (2018).
- [35] M. Serra-Garcia, V. Peri, R. Sustrunk, O. R. Bilal, T. Larsen, L. G. Villanueva, and S. D. Huber, *Observation of a phononic quadrupole topological insulator*, Nature **555**, 342 (2018).
- [36] C. W. Peterson, W. A. Benalcazar, T. L. Hughes, and G. Bahl, *A quantized microwave quadrupole insulator with topologically protected corner states*, Nature **555**, 346 (2018).
- [37] S. Imhof, C. Berger, F. Bayer, J. Brehm, L. W. Molenkamp, T. Kiessling, F. Schindler, C. H. Lee, M. Greiter, T. Neupert and R. Thomale, *Topoelectrical-circuit realization of topological corner modes*, Nat. Phys. **14**, 925 (2018).
- [38] B.-Y. Xie, G.-X. Su, H.-F. Wang, H. Su, X.-P. Shen, P. Zhan, M.-H. Lu, Z.-L. Wang, and Y.-F. Chen, *Visualization of Higher-Order Topological Insulating Phases in Two-Dimensional Dielectric Photonic Crystals*, Phys. Rev. Lett. **122**, 233903 (2019).
- [39] X.-D. Chen, W.-M. Deng, F.-L. Shi, F.-L. Zhao, M. Chen, and J.-W. Dong, *Direct Observation of Corner States in Second-Order Topological Photonic Crystal Slabs*, Phys. Rev. Lett. **122**, 233902 (2019).
- [40] A. El Hassan, F. K. Kunst, A. Moritz, G. Andler, E. J. Bergholtz, and M. Bourennane, *Corner states of light in photonic waveguides*, Nat. Photonics **13**, 697 (2019).
- [41] X. Ni, M. Weiner, A. Alu, and A. B. Khanikaev, *Observation of higher-order topological acoustic states protected by generalized chiral symmetry*, Nat. Mater. **18**, 113 (2019).
- [42] Y. Qi, C. Qiu, M. Xiao, H. He, M. Ke, and Z. Liu, *Acoustic Realization of Quadrupole Topological Insulators*, Phys. Rev. Lett. **124**, 206601 (2020).
- [43] L. Fu, *Topological Crystalline Insulators*, Phys. Rev. Lett. **106**, 106802 (2011).
- [44] T. Neupert and F. Schindler, “Topological crystalline insulators,” in Topological Matter: Lectures from the Topological Matter School 2017, edited by D. Bercioux, J. Cayssol, M. G. Vergniory, and M. Reyes Calvo (Springer International Publishing, Cham, 2018) pp. 31–61.
- [45] C.-A. Li and S.-S. Wu, *Topological states in generalized electric quadrupole insulators*, Phys. Rev. B **101**, 195309 (2020).
- [46] H. Araki, T. Mizoguchi, and Y. Hatsugai, *Phase diagram of a disordered higher-order topological insulator: A machine learning study*, Phys. Rev. B **99**, 085406 (2019).
- [47] Z. Su, Y. Kang, B. Zhang, Z. Zhang, and H. Jiang, *Disorder induced phase transition in magnetic higher-order topological insulator: A machine learning study*, Chin. Phys. B **28**, 117301 (2019).
- [48] C. H. Lee, S. Imhof, C. Berger, F. Bayer, J. Brehm, L. W. Molenkamp, T. Kiessling, and R. Thomale, *Topoelectrical Circuits*, Commun. Phys. **1**, 39 (2018).
- [49] C. Wang and X. R. Wang, (2020), arXiv:2005.06740
- [50] See Supplemental Material at [URL to be added by publisher] for details of (Sec. S1) proof of the quantization of quadrupole moments protected by chiral symmetry; (Sec. S2) effective low-energy edge Hamiltonian and corner modes solution, (Sec. S3) self-consistent Born approximation, (Sec. S4) signatures of disorder induced non-trivial phase, (Sec. S5) the real part of the quadrupole moment formula, (Sec. S6) finite size scaling result, and (Sec. S7) edge Hamiltonian based on lattice model, which includes Refs. [51, 62–64].
- [51] B. Kang, K. Shiozaki, and G. Y. Cho, *Many-body order parameters for multipoles in solids*, Phys. Rev. B **100**, 245134 (2019).
- [52] W. A. Wheeler, L. K. Wagner, and T. L. Hughes, *Many-body electric multipole operators in extended systems*, Phys. Rev. B **100**, 245135 (2019).
- [53] B. Roy, *Antiunitary symmetry protected higher-order topological phases*, Phys. Rev. Research **1**, 032048 (2019).
- [54] C. W. Groth, M. Wimmer, A. R. Akhmerov, J. Tworzydło, and C. W. J. Beenakker, *Theory of the Topological Anderson Insulator*, Phys. Rev. Lett. **103**, 196805 (2009).
- [55] M. J. Park, B. Basa, and M. J. Gilbert, *Disorder-induced phase transitions of type-II Weyl semimetals*, Phys. Rev. B **95**, 094201 (2017).
- [56] C.-Z. Chen, J. Song, H. Jiang, Q.-f. Sun, Z. Wang, and X. C. Xie, *Disorder and Metal-Insulator Transitions in Weyl Semimetals*, Phys. Rev. Lett. **115**, 246603 (2015).
- [57] S. Liu, T. Ohtsuki, and R. Shindou, *Effect of Disorder in a Three-Dimensional Layered Chern Insulator*, Phys. Rev. Lett. **116**, 066401 (2016).
- [58] A. MacKinnon and B. Kramer, *The scaling theory of electrons in disordered solids: Additional numerical results*, Z. Phys. B **53**, 1 (1983).
- [59] B. Kramer and A. MacKinnon, *Localization: theory and experiment*, Rep. Prog. Phys. **53**, 1469 (1993).
- [60] A. Yamakage, K. Nomura, K.-I. Imura, and Y. Kuramoto, *Criticality of the metal-insulator transition driven by disorder*, Phys. Rev. B **87**, 205141 (2013).
- [61] T. Ando, *Electron Localization in a Two-Dimensional System in Strong Magnetic Fields. I. Case of Short-Range Scatterers*, J. Phys. Soc. Jpn. **52**, 1740 (1983).
- [62] S.-Q. Shen, *Topological Insulators: Dirac Equation in Condensed Matter*, 2nd ed. (Springer, Singapore, 2017).
- [63] R. Resta, *Quantum-Mechanical Position Operator in Extended Systems*, Phys. Rev. Lett. **80**, 1800 (1998).
- [64] R. Resta and S. Sorella, *Electron Localization in the Insulating State*, Phys. Rev. Lett. **82**, 370 (1999).

Supplemental materials of “Topological Phase Transitions in Disordered Electric Quadrupole Insulators”

Appendix S1: Proof of the quantization of quadrupole moments protected by chiral symmetry

In this section, we present the proof that the quantization of quadrupole moments is protected by chiral symmetry of the system. The quadrupole moments formula is

$$q_{xy} = \frac{1}{2\pi} \text{Imlog}[\det(U^\dagger \hat{Q} U) \sqrt{\det(\hat{Q}^\dagger)}], \quad (\text{S1.1})$$

where the matrix U is constructed by column-wise packing of the occupied eigenstates, $\hat{Q} = e^{2\pi i \hat{x} \hat{y} / L_x L_y}$, and \hat{x}, \hat{y} are the position operators. To have quantized q_{xy} , the part in the logarithm function has to be real. Thus our target is transformed to prove $\det(U^\dagger \hat{Q} U) \sqrt{\det(\hat{Q}^\dagger)}$ is real.

To this end, we perform a deformation of the determinant as

$$\begin{aligned} \det(U^\dagger \hat{Q} U) &= \det[U^\dagger (\hat{Q} - \mathbf{1} + \mathbf{1}) U] \\ &= \det[\mathbf{1} + U^\dagger (\hat{Q} - \mathbf{1}) U]. \end{aligned} \quad (\text{S1.2})$$

Using the Sylvester's determinant identity $\det(\mathbf{1} + AB) = \det(\mathbf{1} + BA)$, the above equation is simplified to be

$$\det(U^\dagger \hat{Q} U) = \det(\mathbf{1} + (\hat{Q} - \mathbf{1}) U U^\dagger). \quad (\text{S1.3})$$

Note that $U U^\dagger = P_{\text{occ}}$ is the projection operator projected to occupied states, and $P_{\text{occ}} = \mathbf{1} - V V^\dagger$ where V is constructed by the unoccupied states. Thus

$$\begin{aligned} \det(U^\dagger \hat{Q} U) &= \det[\mathbf{1} + (\hat{Q} - \mathbf{1})(\mathbf{1} - V V^\dagger)] \\ &= \det[\hat{Q} - (\hat{Q} - \mathbf{1}) V V^\dagger] \\ &= \det[\mathbf{1} + (\hat{Q}^\dagger - \mathbf{1}) V V^\dagger] \det \hat{Q} \\ &= \det(V^\dagger \hat{Q}^\dagger V) \det \hat{Q}. \end{aligned} \quad (\text{S1.4})$$

Let us focus on the system with chiral symmetry. If the system respects chiral symmetry, i.e., $\gamma_5^{-1} H \gamma_5 = -H$, the occupied states and unoccupied states are related by chiral symmetry operator as

$$V = \gamma_5 U. \quad (\text{S1.5})$$

Utilize this relation and note that $[\gamma_5, \hat{Q}] = 0$, we have

$$\begin{aligned} \det(U^\dagger \hat{Q} U) &= \det(V^\dagger \hat{Q}^\dagger V) \det \hat{Q} \\ &= \det(U^\dagger \gamma_5^\dagger \hat{Q}^\dagger \gamma_5 U) \det \hat{Q} \\ &= \det(U^\dagger \hat{Q}^\dagger U) \det \hat{Q}. \end{aligned} \quad (\text{S1.6})$$

As the matrix \hat{Q} is unitary, we have

$$\det(U^\dagger \hat{Q} U) \sqrt{\det \hat{Q}^\dagger} = \det(U^\dagger \hat{Q}^\dagger U) \sqrt{\det \hat{Q}}, \quad (\text{S1.7})$$

thus

$$\det(U^\dagger \hat{Q} U) \sqrt{\det \hat{Q}^\dagger} = \left(\det(U^\dagger \hat{Q} U) \sqrt{\det \hat{Q}^\dagger} \right)^*, \quad (\text{S1.8})$$

Finally, the determinant $\det(U^\dagger \hat{Q} U) \sqrt{\det \hat{Q}^\dagger}$ is real. It is proved that q_{xy} is quantized to 0 or $\frac{1}{2}$.

Actually, the above conclusion can be generalized to system with particle-hole symmetry. The particle-hole symmetry operator is represented by an anti-unitary operator $P = U_p K$ where U_p is a unitary matrix and K represents complex conjugation. Thus the occupied states and unoccupied states are related by the particle-hole symmetry operator as

$$V = P U = U_p K U = U_p U^*. \quad (\text{S1.9})$$

Then following the above formula, we have

$$\begin{aligned}
\det(U^\dagger \hat{Q} U) &= \det(U^T U_p^\dagger \hat{Q}^\dagger U_p U^*) \det \hat{Q} \\
&= \det(U^T \hat{Q}^\dagger U^*) \det \hat{Q} \\
&= \det(U^\dagger \hat{Q}^T U)^* \det \hat{Q} \\
&= \det(U^\dagger \hat{Q} U)^* \det \hat{Q}.
\end{aligned} \tag{S1.10}$$

Finally, we still have

$$\det(U^\dagger \hat{Q} U) \sqrt{\det \hat{Q}^\dagger} = \left(\det(U^\dagger \hat{Q} U) \sqrt{\det \hat{Q}^\dagger} \right)^* . \tag{S1.11}$$

It is proved that q_{xy} is also quantized to 0 or $\frac{1}{2}$ by particle-hole symmetry.

Appendix S2: Effective low-energy edge Hamiltonian and corner modes solution

In this section, we derive the low-energy edge Hamiltonian for the quantized electric quadrupole insulators. For the chosen parameters, the bulk gap closes at the $(k_x, k_y) = (\pi, \pi)$ point when $t_x = t_y = 1$. Expanding Eq. (1) in the main text around this gap closing point to the second order, we have an effective model

$$H(\mathbf{k}) = k_y \gamma_1 + M_y \gamma_2 + k_x \gamma_3 + M_x \gamma_4, \tag{S2.1}$$

where $M_{x,y} \equiv m_{x,y} - b k_{x,y}^2$ and $m_{x,y} \equiv 1 - t_{x,y}$, and $b = \frac{1}{2}$. Note that an overall minus sign is neglected. This effective bulk Hamiltonian inherits all symmetries of the original model.

The target is to get an effective edge Hamiltonian starting from this effective bulk Hamiltonian. To this end, let us consider a semi-infinite plain $x \geq 0$ and keep k_y a good quantum number. The wave function thus has a form $\Psi(x, k_y) = \psi(x) e^{i k_y y}$. Then the Schrödinger equation $H(\mathbf{k}) \Psi(x, k_y) = E \Psi(x, k_y)$ leads to

$$[-i \partial_x \gamma_3 + M_x \gamma_4] \psi(x) + (k_y \gamma_1 + M_y \gamma_2) \psi(x) = E \psi(x), \tag{S2.2}$$

where we have replaced $k_x \rightarrow -i \partial_x$, and E is the energy. The first parentheses has grouped all the dependence on the x coordinate, and this equation can have solution only if the first parentheses gives constant. For simplicity we set this constant to be zero and obtain

$$(-i \partial_x + M_x \gamma_3 \gamma_4) \psi(x) = 0. \tag{S2.3}$$

Simplifying it further,

$$\partial_x \psi(x) = M_x \tau_3 \sigma_3 \psi(x). \tag{S2.4}$$

Thus $\psi(x)$ should be an eigen function of $\tau_3 \sigma_3$ as $\psi(x) = \phi(x) \chi_{\tau, \sigma}$ where $\tau_3 \sigma_3 \chi_{\tau, \sigma} = \tau \sigma \chi_{\tau, \sigma}$ with $\tau, \sigma = \pm 1$. Taking the trial wave function $\phi(x) = e^{-\zeta x}$, we have the secular equation

$$b \zeta^2 - \tau \sigma \zeta + m_x = 0. \tag{S2.5}$$

The two roots are $\zeta_{1,2} = \frac{\tau \sigma \pm \sqrt{1 - 4 m_x b}}{2b}$, and they satisfy the relation

$$\zeta_1 + \zeta_2 = \frac{\tau \sigma}{b}, \zeta_1 \zeta_2 = \frac{m_x}{b}. \tag{S2.6}$$

To have edge states, the two roots should be positive, which constrains the condition

$$m_x > 0, \sigma = \text{sgn}(\tau). \tag{S2.7}$$

Under this constraint, then $\chi_{\tau, \sigma}$ is reduced to positive eigenvalues as $\tau_3 \sigma_3 \chi_{\tau, \sigma} = +1 \chi_{\tau, \sigma}$. The spatial part of wave functions are now $\phi(x) = C(e^{-\zeta_1 x} - e^{-\zeta_2 x})$ where C is a normalization factor.

Now we have two states $\psi_+ = \chi_{\tau=1, \sigma=1} \phi(x)$ and $\psi_- = \chi_{\tau=-1, \sigma=-1} \phi(x)$. Then projecting the remaining part of the Hamiltonian into the subspace spanned by these two states, we find the effective edge Hamiltonian along the y direction as

$$H_{\text{edge}}(k_y) = (m_y - bk_y^2)\rho_x - k_y\rho_y, \quad (\text{S2.8})$$

where $\rho_{x,y}$ are the Pauli matrices in the basis $\{\psi_+, \psi_-\}$. This Hamiltonian describes exactly the one-dimensional Dirac Hamiltonian [62]. It is topologically nontrivial if $\text{sgn}(m_y b) > 0$ and topologically trivial if $\text{sgn}(m_y b) < 0$. This result is consistent with the phase diagram of quantized electric quadrupole insulators. Take a similar approach, the effective edge Hamiltonian along the x direction is

$$H_{\text{edge}}(k_x) = (m_x - bk_x^2)\rho_x - k_x\rho_y. \quad (\text{S2.9})$$

Next we present the solution of corner modes starting again from the bulk effective mode. Consider the zero-energy states at the corner $x, y \geq 0$. The corner modes are assumed to be

$$\Psi_c(x, y) = \chi_c \phi_x(x) \phi_y(y), \quad (\text{S2.10})$$

which should satisfy the boundary condition

$$\Psi_c(x=0, y) = \Psi_c(x, y=0) = \Psi_c(x=\infty, y=\infty) = 0. \quad (\text{S2.11})$$

Then the Schrödinger equation $H(\mathbf{k})\Psi_c(x, y) = 0$ leads to

$$\begin{aligned} (-i\partial_x + M_x\gamma_3\gamma_4)\chi_c\phi_x(x) &= 0, \\ (-i\partial_y + M_y\gamma_1\gamma_2)\chi_c\phi_y(y) &= 0. \end{aligned}$$

These two equations together with the boundary conditions require

$$\gamma_1\gamma_2\chi_c = +i\chi_c, \quad \gamma_3\gamma_4\chi_c = +i\chi_c. \quad (\text{S2.12})$$

Using the relation $\gamma_5 = \tau_3\sigma_0$ and $\gamma_1\gamma_2\gamma_3\gamma_4\gamma_5 = -1$, we note that χ_c is the eigen state of γ_5 as

$$\gamma_5\chi_c = +1\chi_c. \quad (\text{S2.13})$$

Combining with the condition Eq. S2.12, we only have

$$\chi_c = (1, 0, 0, 0)^T. \quad (\text{S2.14})$$

Finally, the corner mode is

$$\Psi(x, y) = C\chi_c(e^{-\zeta_1 x} - e^{-\zeta_2 x})(e^{-\lambda_1 y} - e^{-\lambda_2 y}), \quad (\text{S2.15})$$

where C is a normalization factor, $\zeta_{1,2} = \frac{1 \pm \sqrt{1-4m_x b}}{2b}$, and $\lambda_{1,2} = \frac{1 \pm \sqrt{1-4m_y b}}{2b}$.

For a square sample, the other two neighboring corner modes are eigenstates of γ_5 with eigenvalue -1 as $\gamma_5\chi_c = -1\chi_c$.

Appendix S3: Self-consistent Born approximation analysis

In this section, we provide some details for the self-consistent Born approximation (SCBA) analysis. We start from the clean Hamiltonian, as Eq. (1) in the main text,

$$\begin{aligned} H_q(\mathbf{k}) &= t \sin k_y \gamma_1 + [t_y + t \cos k_y] \gamma_2 \\ &\quad + t \sin k_x \gamma_3 + [t_x + t \cos k_x] \gamma_4 \end{aligned} \quad (\text{S3.1})$$

where the gamma matrices are $\gamma_j \equiv -\tau_2 \sigma_j$ ($j = 1, 2, 3$) and $\gamma_4 \equiv \tau_1 \sigma_0$ with τ and σ both being Pauli matrices but for different degrees of freedom. The model parameters $t_{x,y}$ and t are defined the same as in the main text. In our case we consider the disorder with the form $V(\mathbf{r})\gamma_4$, the full Hamiltonian is

$$\mathcal{H} = H_q(\mathbf{k}) + V(\mathbf{r})\gamma_4, \quad (\text{S3.2})$$

where the potential $V(\mathbf{r})$ distributes uniformly within the interval $[-W/2, W/2]$.

Then the effects of disorder can be accounted in terms of the self-energy defined as

$$\frac{1}{E_F - H_q(\mathbf{k}) - \Sigma(E_F)} = \langle \frac{1}{E_F - \mathcal{H}} \rangle, \quad (\text{S3.3})$$

where $\langle \dots \rangle$ denotes the average over all disorder configurations. Consider the symmetry of the Hamiltonian and Brillouin zone, the self-energy is simplified to a form

$$\Sigma(E_F) = \Sigma_4 \gamma_4 + \Sigma_2 \gamma_2 + \Sigma_0 I_{4 \times 4}. \quad (\text{S3.4})$$

E_F is Fermi energy and it is set as zero in our following discussion.

The key is to get self-energy self-consistently, which will renormalize the original Hamiltonian. Note that the real part of self-energy renormalizes parameters of original Hamiltonian, while the its imaginary parts give band broadening and life time of quasiparticles. In the self-consistent Born approximation, the self-energy Σ is given by the integral equation

$$\Sigma = \frac{W^2}{48\pi^2} \int_{BZ} d^2\mathbf{k} \gamma_4 \frac{1}{E_F + i\delta - H_q(\mathbf{k}) - \Sigma} \gamma_4, \quad (\text{S3.5})$$

where the integral runs over the first Brillouin zone, and δ is an infinitesimal positive number. From Eq. (S3.5), there are explicitly three coupled self-consistent integral equations

$$\begin{aligned} \Sigma_0 &= \frac{W^2}{12} \frac{a^2}{4\pi^2} \int_{BZ} d^2\mathbf{k} \frac{i\delta - \Sigma_0}{(i\delta - \Sigma_0)^2 - E^2(k)}, \\ \Sigma_4 &= \frac{W^2}{12} \frac{a^2}{4\pi^2} \int_{BZ} d^2\mathbf{k} \frac{t_x + t \cos k_x + \Sigma_4}{(i\delta - \Sigma_0)^2 - E^2(k)}, \\ \Sigma_2 &= -\frac{W^2}{12} \frac{a^2}{4\pi^2} \int_{BZ} d^2\mathbf{k} \frac{t_y + t \cos k_y + \Sigma_2}{(i\delta - \Sigma_0)^2 - E^2(k)}, \end{aligned} \quad (\text{S3.6})$$

where $E^2(k) = (\Sigma_4 + t_x)^2 + 2(\Sigma_4 + t_x)t \cos k_x + t^2 + (\Sigma_2 + t_y)^2 + 2(\Sigma_2 + t_y)t \cos k_y + t^2$.

After obtaining the self-energy Σ , the mass terms are renormalized to

$$\begin{aligned} \bar{t}_x &= t_x + \text{Re}\Sigma_4, \\ \bar{t}_y &= t_y + \text{Re}\Sigma_2. \end{aligned} \quad (\text{S3.7})$$

Then the phase boundary of topological quadrupole insulators is reset at

$$|\bar{t}_x| = |\bar{t}_y| = 1. \quad (\text{S3.8})$$

As discussed in the main text on the phase diagram Fig. 1(b), the upper horizontal phase boundary is nearly flat thus it shows little dependence on t_x . Indeed, this observation is true, which is verified by the self-consistent Born approximation, as shown in Fig. S1(a). And we can take the similar approach to the phase boundary along t_y direction. From the integral equations, one can find it also shows little dependence on t_y .

Appendix S4: Signatures of disorder induced nontrivial phase

In this section, we show explicitly the corner charges and zero-energy modes in the disorder-induced topological Anderson phase in electric quadrupole insulators. Corresponding to the phase diagram Fig. 1(b) in the main text, we choose two scenarios to illustrate our points: $t_x = 0.9$ and $t_x = 1.05$.

For the first scenario, $q_{xy} = 1/2$ for $W = 0$. In the limit $W \rightarrow \infty$, $W\gamma_4$ term dominates and hence $q_{xy} = 0$. As such, there must exist a topological phase transition as increasing the disorder strength W . The varying of q_{xy} as function W is shown in Fig. S2(a), where one finds that q_{xy} stays quantized and has no fluctuations even for quite large W (compared to edge band gap, see the section S7), and no disorder average is necessary. At this moment, the zero-energy modes (see Fig. S2(c)) and quantized corner charges (see Fig. S2(e)) are robust against disorders. Around the critical point $W_c \simeq 3$, the q_{xy} suddenly switch from $q_{xy} = 1/2$ to $q_{xy} = 0$, accompanied by strong fluctuations during this phase transition.

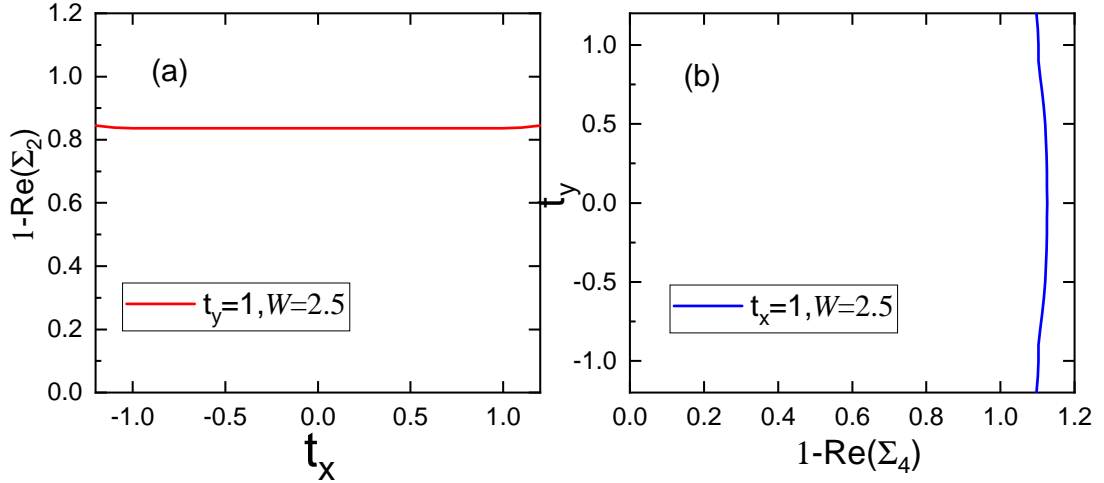


Figure S1. Self-consistent Born analysis of phase boundaries. (a) Insensitivity of modification $\text{Re}[\Sigma_2]$ as changing parameter t_x . (b) Insensitivity of modification $\text{Re}[\Sigma_4]$ as changing parameter t_y .

For the second scenario, $q_{xy} = 0$ for $W = 0$. Similarly, in the limit $W \rightarrow \infty$, $q_{xy} = 0$. The difference is that by increasing the strength, the disorder can gradually drive q_{xy} away from zero and reach the value near one-half, then decay to zero finally, see Fig. S2(b). This process indicates a topological phase transition driven by disorder from trivial phase to nontrivial phase. Finally the system is back to trivial phase again. The appearance of the nontrivial phase induced by disorders is evidenced by the zero-energy modes (see Fig. S2(d)). The corresponding corner charge (see Fig. S2(f)) approaches to quantized values as the system size is large enough.

Appendix S5: The real part of quadrupole moments formula

In this section, we use information obtained from the real part of quadrupole moments formula to detect phase boundaries. From Resta's construction [63, 64], besides the fact that imaginary part of $\det(U^\dagger \hat{P} U)$ gives rise the polarization, its real part also provides useful information, i.e., the localization length of ground states (note that $\hat{P} = \exp[i2\pi\hat{x}/L_x]$). Taking a close analogy, the real part of $\det(U^\dagger \hat{Q} U)$ should also provide invaluable information. Here we define the “localization length” of ground states in electric quadrupole insulators as [64]

$$\xi = -\text{Re} \log \det(U^\dagger \hat{Q} U). \quad (\text{S5.1})$$

Let us first verify that ξ calculated from Eq. (S5.1) can be used to detect phase transition. In Fig. S3(a), we compare the scaling behavior of ξ for different sample size in the clean system. Note that ξ is scaled by factor of $\log L$ in Fig. S3 by considering finite size scaling [51]. Two features in Fig. S3(a) are obvious. First, a peak stands approximately at $t_x = 1$, which is the phase boundary as we know from phase diagram. When $t_x < 1$, the system is in topological nontrivial phase, and when $t_x > 1$, the system is trivial. Second, the peak becomes higher and approaches closer to $t_x = 1$ as system size is enlarged. One can expect that the position of the peak finally locates at $t_x = 1$, and its peak values of ξ approaches to infinity in the thermodynamic limit. Thus, based on this peak position, we may identify the phase boundary.

Then let us turn to the case of disordered systems, as shown in Fig. S3(b). Here two typical scenarios of phase transition are exemplified to illustrate our points. In the first scenario [see pink line in Fig. S3(b)], disorder drives the system directly from topological quadrupole insulator to a trivial insulator. In this case, ξ nearly keeps a constant with negligible fluctuations, like a plateau, for small W , and one may treat this robustness feature of ξ as a signature of topological nontrivial phase. As the increasing of W , ξ strikes a peak at critical value $W_{c1} = 2.9$ at which the topological phase transition occurs. While in the second scenario [see orange line in Fig. S3(b)], the system starts from trivial phase and experiences a disorder-induced topological Anderson phase before entering the trivial phase under sufficiently strong disorder. As the increasing of W in this case, ξ first grows to a plateau then also experiences a peak. Actually, the first phase transition from trivial to nontrivial phase is vaguely captured by a small peak [see the left dashed line], and the narrow plateau afterwards solidifies the existence of topological nontrivial phase. While

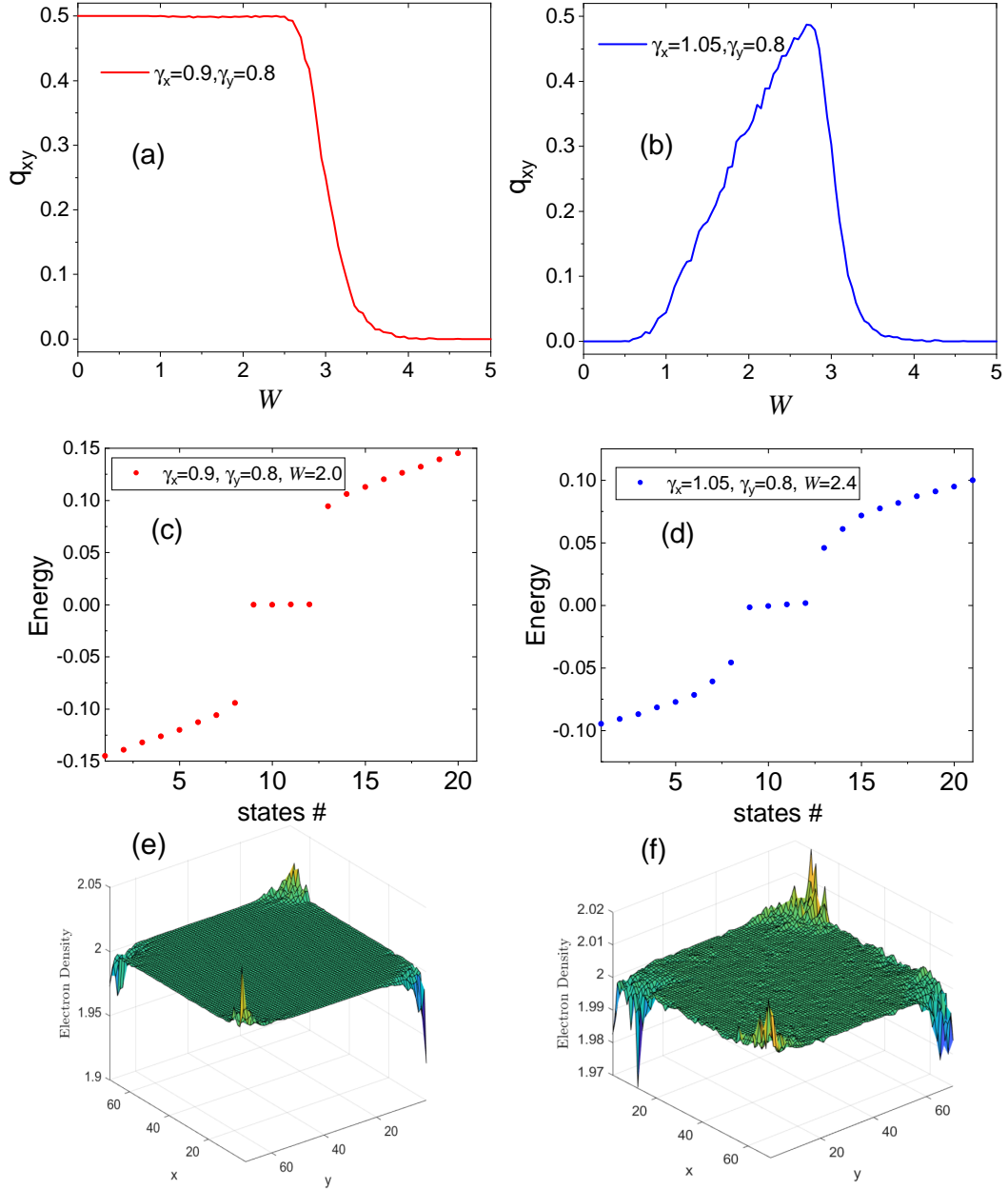


Figure S2. Signature of disorder-driven nontrivial phase in electric quadrupole insulators. (a,b) Evolution of quadrupole moments q_{xy} with disorder strength W . Periodic boundary condition is taken and 1000 disorder configurations are made. (c,d) The energy modes near the zero energy. (e,f) Electron charge density corresponds to (c,d), respectively; the system size is $L_x \times L_y = 70 \times 70$, and open boundary condition is taken. Here, only one disorder configuration is taken in (e,f).

the followed peak of ξ clearly indicates the phase boundary. Concluding from both scenarios, the phase boundary between trivial and nontrivial phases locates at $W_{c2} \simeq 2.96$, which is consistent with the phase diagram in Fig. 1 in the main text. As we can see, the calculation of ξ works as a complement to phase boundary in Fig. 1 in the main text. If we consider a third scenario, say $t_x = 1.5$ in Fig. S1, it is found that ξ grows all the way following W from 0 to 4 and shows no sign of peak, which is also consistent with the phase diagram.

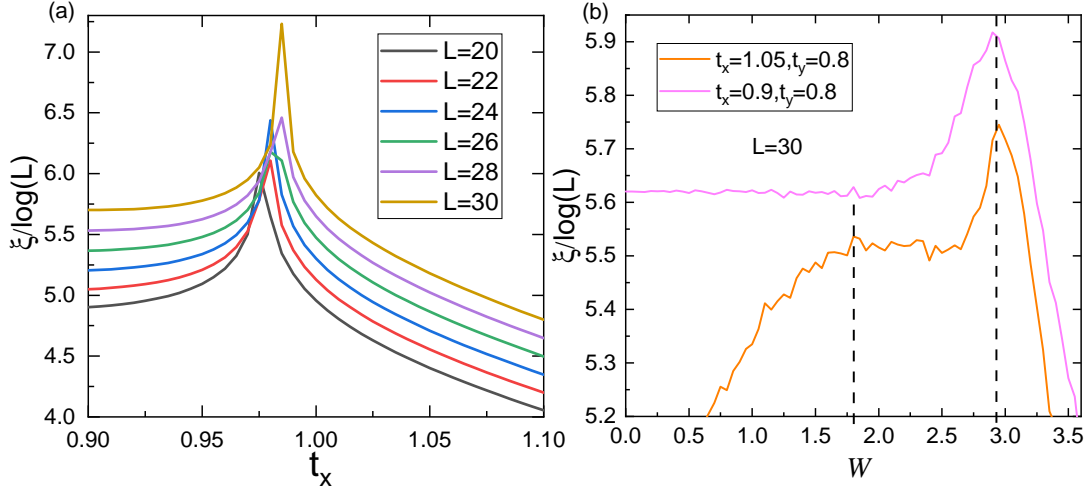


Figure S3. Phase transition of electric quadrupole insulators indicated by the localization length. (a) ξ as function of t_x for different system size in the clean case. Here $t_y = 0.75$. (b) ξ as function of disorder strength W . The system size is set as $L \equiv L_x = L_y = 30$, and 1000 disorder configurations are taken.

Appendix S6: Finite size scaling result

In this section, we explore the signatures of delocalized states at the sample boundaries as consequence of disorder-driven topological phase transitions. Consider a long ribbon (2×10^6 in units of lattice constant) along the x direction. The localization length is calculated using the transfer matrix method. For the single-parameter scaling, we plot the dimensionless localization length Λ/L_y as functions of disorder strength W (or parameter t_x) in Fig. S4. As we discussed in the main text, since the bulk is always trivial, finite size scaling with periodic boundary condition (along the transverse direction of the ribbon) cannot reveal the topological phase transitions of the electric quadrupole insulators, as shown in Fig. S4(a). Then we try the case with open boundary condition. From the finite size scaling theory, the dimensionless localization length Λ_x/L_y becomes scale free near the critical point of metal-insulator transition. For the case of $t_x = t_y = 0.8$, a phase transition occurs during the increasing of W (see Fig. 1 in the main text), while the finite size scaling result in Fig. S4(b) shows no critical point, and thus the bulk and boundaries along the x direction show insulating behavior. If we tune the parameters to $t_x = 1.1, t_y = 0.8$, it seems that two “critical points” W_{c1} and W_{c2} occur during the increasing of W , and the region between W_{c1} and W_{c2} exhibit a metallic behavior. While this signature is “false” since as increasing the width L_y further, the two “critical points” approach to phase boundary point W_c simultaneously, at which the localization length Λ_x diverges (see Fig. S4(c)). To verify this point, we take t_x instead of W as the scaling parameter in Fig. S4(d). Similarly, the two “critical points” will approach to the phase boundary point as increasing the width L_y .

Appendix S7: The edge Hamiltonian based on lattice model

In this section, we derive the exact edge Hamiltonian based on the lattice model. Let us first observe the energy band of an infinitely long ribbon along the x direction but with finite width in the y direction, as shown in Fig. S5(a). The red lines indicates the edge bands whose wave function localized at the edges. It is interesting to find that these edge bands, unlike other bulk bands, do not shift as varying t_y as long as $|t_y| < 1$ [see Fig. S5(b)]. Under the condition $|t_y| < 1$, the edge band gap is

$$E_{gx} = 2|1 - t_x|. \quad (\text{S7.1})$$

In the following we derive the exact form of the edge Hamiltonian, which will give the edge band gap naturally. Assume the ribbon width is N_y and take open boundary condition at y direction. By partial Fourier transformation

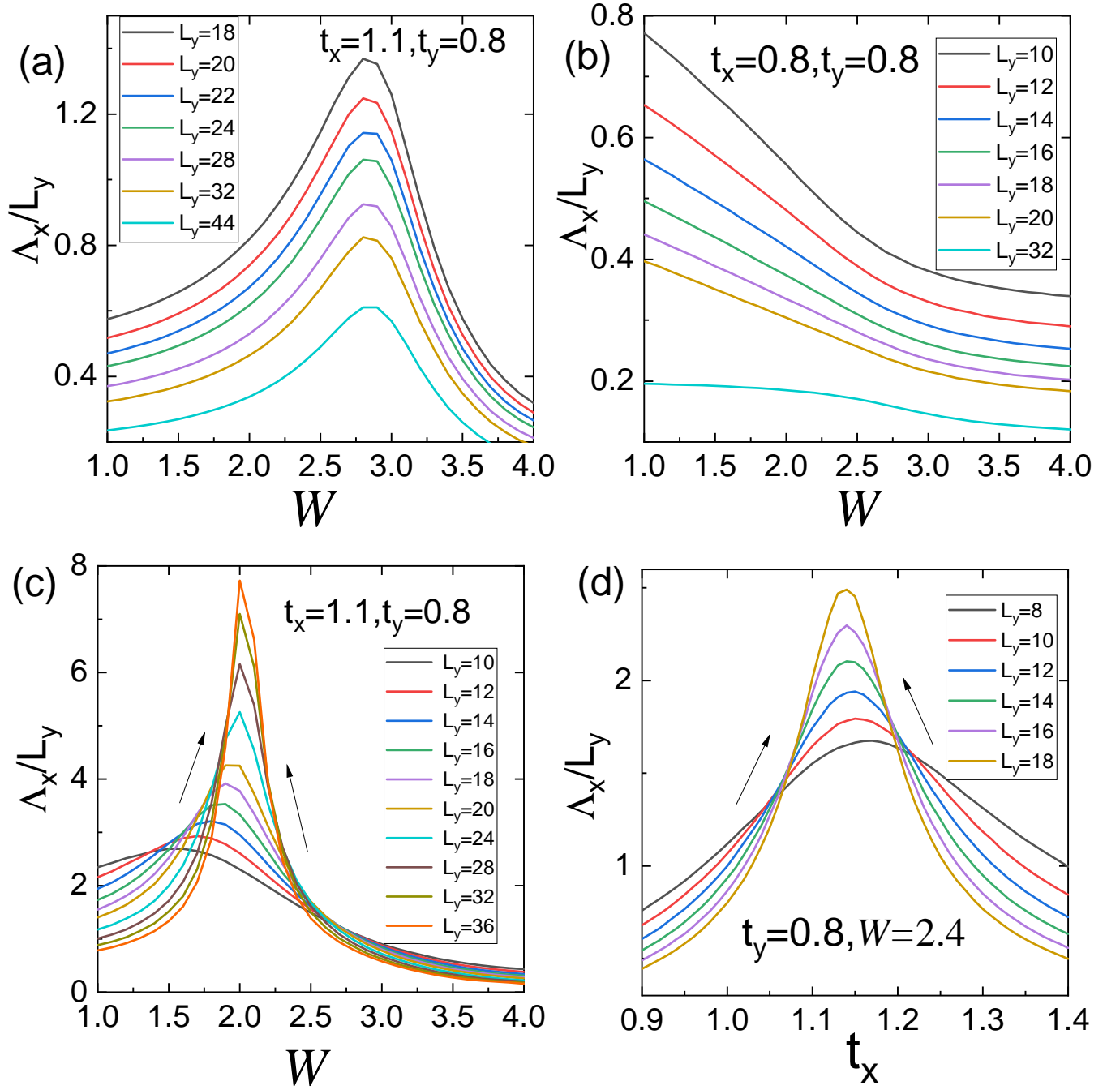


Figure S4. Dimensionless localization length for different cases corresponding to the phase diagram Fig. 1 in the main text. The periodic boundary condition is only applied to (a).

of the lattice Hamiltonian along the x direction, it reads

$$H = \sum_{k_x} \left[\sum_{R_j=1}^{N_y} \Psi_{k_x, R_j}^\dagger h_{j,j}(k_x) \Psi_{k_x, R_j} + \sum_{R_j=1}^{N_y-1} \Psi_{k_x, R_j}^\dagger h_{j,j+1}(k_x) \Psi_{k_x, R_j+1} + h.c. \right], \quad (\text{S7.2})$$

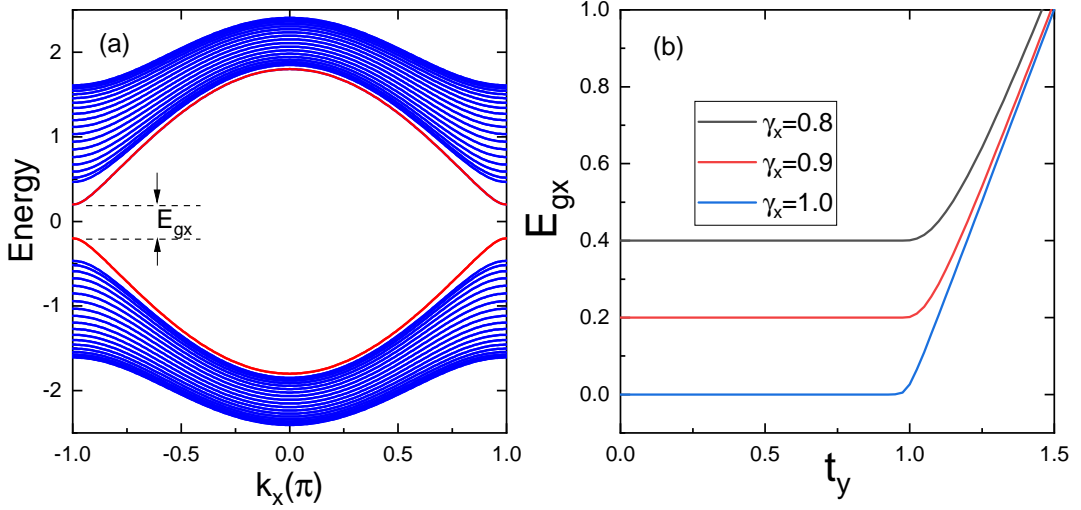


Figure S5. The edge band gap. (a) Energy spectrum for $t_x = 0.8, t_y = 0.6$. (b) Edge band gap as function of t_y .

where

$$h_{j,j}(k_x) = \begin{pmatrix} 0 & 0 & t_x + te^{ik_x} & t_y \\ 0 & 0 & -t_y & t_x + te^{-ik_x} \\ t_x + te^{-ik_x} & -t_y & 0 & 0 \\ t_y & t_x + te^{ik_x} & 0 & 0 \end{pmatrix}, h_{j,j+1}(k_x) = \begin{pmatrix} 0 & 0 & 0 & t \\ 0 & 0 & 0 & 0 \\ 0 & -t & 0 & 0 \\ 0 & 0 & 0 & 0 \end{pmatrix}, \quad (S7.3)$$

and $\Psi_{k_x, R_j} = [C_{k_x, R_j, 1}, C_{k_x, R_j, 2}, C_{k_x, R_j, 3}, C_{k_x, R_j, 4}]^T$.

We note that Eq. (S7.2) describes a four-band Su-Schrieffer-Heeger (SSH) chain along the y direction with open boundary. In the case of $t = 1$, it is topologically nontrivial when $|t_y| < 1$. Thus it gives the end states as $E_{\text{edge}}(k_x, t_x)$, which is exactly the edge band indicated by red line in Fig. S5(a). Usually, it is hard to get the $E_{\text{edge}}(k_x, t_x)$ for general t_y , but let us focus on the simplest case $t_y = 0$, at which the four-band SSH chain decouples to a block diagonal form

$$H = \text{diag}(H_{\text{SSH}, x}, B, B, \dots, B, H_{\text{SSH}, x}), \quad (S7.4)$$

where

$$H_{\text{SSH}, x} = \begin{pmatrix} 0 & t_x + te^{-ik_x} \\ t_x + te^{ik_x} & 0 \end{pmatrix}, B = \begin{pmatrix} 0 & t_x + te^{ik_x} & 0 & t \\ t_x + te^{-ik_x} & 0 & -t & 0 \\ 0 & -t & 0 & t_x + te^{-ik_x} \\ t & 0 & t_x + te^{ik_x} & 0 \end{pmatrix}. \quad (S7.5)$$

At this point, we totally dimerized the Hamiltonian, and the end modes are encoded in the two matrices $H_{\text{SSH}, x}$ at the ends of the chain, and we find that $H_{\text{SSH}, x}$ is exactly the SSH model. By diagonalizing $H_{\text{SSH}, x}$, such that

$$E_{\text{edge}}(k_x, t_x) = \pm \sqrt{t_x^2 + t^2 + 2t_x t \cos k_x}, \quad (S7.6)$$

which gives the edge bands as denoted by the red lines in Fig. S5(a).

For $t_y \neq 0$, the Hamiltonian Eq. (S7.2) cannot be totally dimerized thus is difficult to solve. Now we consider a semi-infinite plane with $y \geq 0$ and keep k_x good quantum number. Assume the edge states wave function

$$\psi(R_i^x, R_j^y) = \frac{1}{\sqrt{N_y}} e^{ik_x R_i^x} \phi(R_j^y), \quad (S7.7)$$

where $\phi(R_j^y)$ is the spatial part along the y direction that contains the decay factors. By projecting out the degrees of freedom R_j^y , we have an effective lattice model on the x direction. The hopping integrals between sites $R_{i,A}^x$ and $R_{i,B}^x$ is obtained as

$$\sum_{R_j^y} \psi^*(R_{i,A}^x, R_j^y) t_x \psi(R_{i,B}^x, R_j^y) = t_x, \quad (\text{S7.8})$$

and the hopping integrals between sites $R_{i,B}^x$ and $R_{i+1,A}^x$ is obtained as

$$\sum_{R_j^y} \psi^*(R_{i,B}^x, R_j^y) t \psi(R_{i+1,A}^x, R_j^y) = t e^{ik_x}. \quad (\text{S7.9})$$

Thus the effective lattice model on the x direction is still the same SSH model as

$$H_{\text{SSH},x} = \begin{pmatrix} 0 & t_x + t e^{-ik_x} \\ t_x + t e^{ik_x} & 0 \end{pmatrix} \quad (\text{S7.10})$$

under the basis $(C_{k_x,A}, C_{k_x,B})^T$ where $C_{k_x,A/B}$ is the annihilation operator. It is numerically verified true that the edge bands should remain the same no matter what t_y is when $|t_y| < 1$. At $k_x = \pi$, it gives the edge band gap E_{gx} as stated before. For $|t_y| > 1$, no edge bands exist.

If we focus on the edge band along the y direction, we have the similar result as

$$H_{\text{SSH},y} = \begin{pmatrix} 0 & t_y + t e^{-ik_y} \\ t_y + t e^{ik_y} & 0 \end{pmatrix}, \quad (\text{S7.11})$$

and corresponding edge bands

$$E_{\text{edge}}(k_y, t_y) = \pm \sqrt{t_y^2 + t^2 + 2t_y t \cos k_y}. \quad (\text{S7.12})$$
